

# PREPARATION AND CHARACTERIZATION OF P-N HETEROJUNCTION $\text{CuBi}_2\text{O}_4/\text{CeO}_2$ AND ITS PHOTOCATALYTIC ACTIVITIES UNDER UVA LIGHT IRRADIATION

A. Elaziouti <sup>1,2</sup>, N. Laouedj <sup>1,2</sup>, A. Bekka <sup>1</sup> and RN. Vannier <sup>3</sup>

<sup>1</sup> LCMIA Laboratory of Inorganic Materials Chemistry and Application, Department of Physical Chemistry, University of the Science and the technology of Oran (USTO M.B), Oran, Algeria

<sup>2</sup> Dr. Moulay Tahar University, Saida, Algeria.

<sup>3</sup> Unit of Catalysis and Solid State Chemistry of Lille University, Lille, France.

<sup>1</sup>E-mail : elaziouti\_a@yahoo.com

Reçu le 12/05/2014 – Accepté le 24/06/2014

## Résumé

Les matériaux composites  $\text{CuBi}_2\text{O}_4/\text{CeO}_2$  ont été synthétisés par voie des réactions à l'état solide puis caractérisés par la diffraction des rayons X, la microscopie électronique à balayage et la spectroscopie UV-Visible en mode de réflectance diffuse. L'efficacité photocatalytique de ces matériaux sous irradiation UVA vis-à-vis de l'élimination d'un polluant modèle en l'occurrence : le rouge Congo (RC). Le photocatalyseur en  $\text{CuBi}_2\text{O}_4/\text{CeO}_2$  présentait un taux de conversion de polluant de 83,05 % au bout de 100 min de temps d'irradiation avec 30 % de  $\text{CuBi}_2\text{O}_4$  à l'ambiance et à pH 7. Les réactions de photodégradation étaient satisfaisantes en corrélation avec le modèle cinétique de pseudo-premier ordre. Le mécanisme de l'efficacité photocatalytique amélioré a été expliqué par la charge modèle de séparation à hétérojonction.

**Mots clé :**  $\text{CuBi}_2\text{O}_4/\text{CeO}_2$ , hétérojonction, rouge Congo, efficacité photocatalytique, effet synergétique.

## Abstract

$\text{CuBi}_2\text{O}_4/\text{CeO}_2$  composite materials were synthesized by solid state method and were characterized by a number of techniques such as X-ray diffraction, scanning electron microscopy and UV-Vis diffuse reflectance spectroscopy. The photocatalytic activity of the materials was investigated under UVA light and assessed using Congo red (CR) dye as probe reaction. The  $\text{CuBi}_2\text{O}_4/\text{CeO}_2$  photocatalyst exhibited the high efficiency as a result of 83.05% of decomposition of CR for 100 min of irradiation time with 30 wt % of  $\text{CuBi}_2\text{O}_4$  at room temperature and a pH 7. The photodegradation reactions were satisfactory correlated with the pseudo-first-order kinetic model. The mechanism of the enhanced photocatalytic efficiency was explained by the heterojunction charge separation model.

**Key words:**  $\text{CuBi}_2\text{O}_4/\text{CeO}_2$  heterojunction, Congo red, photocatalytic activity, synergy effect.

## ملخص

حضرت المواد المركبة  $\text{CuBi}_2\text{O}_4/\text{CeO}_2$  حسب طريقة الحالة الصلبة وتميزت بعدد من تقنيات مثل حيود الأشعة السينية، المجهر الإلكتروني والأشعة فوق البنفسجية في مواجهة منتشر الانعكاس الطيفي. وكان التحقيق في النشاط الحفز الضوئي تحت الضوء فوق البنفسجية وتقييمها باستخدام صبغ الكونغو الحمراء (CR) كنموذج تفاعل. أظهرت نتيجة نشاط الحفز الضوئي  $\text{CuBi}_2\text{O}_4/\text{CeO}_2$  كفاءة عالية بمعدل تفكك 83.05% من الملوثات لمدة 100 دقيقة من الوقت الإشعاع مع 30%  $\text{CuBi}_2\text{O}_4$  في درجة حرارة الغرفة ودرجة الحموضة 7. النشاط الحفز الضوئي مناسبة لنموذج الحركية من الدرجة الأولى. آلية تعزيز نشاط الحفز الضوئي من قبل نموذج انفصال الشحن في التوصيل غير متجانس.

## الكلمات المفتاحية

التوصيل غير متجانس , الكونغو الحمراء , النشاط الحفز الضوئي , تأثير التآزر

## 1- INTRODUCTION

The lanthanide cerium dioxide ( $\text{CeO}_2$ ) has been attracting great interest in the recent years because of its effective technological applications, such as in solid-state electrolytes for electrochemical devices [1,2] catalysts for three-way automobile exhaust systems [3,4], abrasives for chemical-mechanical planarization [5], sunscreens for ultraviolet absorbents [6], the adsorption and reaction of formaldehyde [7], oxygen storage capacity [8], hybrid solar cells [9],  $\text{H}_2\text{S}$  removal [10] and luminescent materials for violet/blue fluorescence [11]. Cubic fluorite cerium dioxide ( $\text{CeO}_2$ ), a semiconductor with a relatively narrow band gap of 2.7 and 3.4 eV depending to the technique of preparation [12], shows promising photocatalytic activity for the degradation of various organic dye pollutants such as Methylene Blue (MB), Methyl Orange (MO) and C.I. Reactive Black 5 (RB5) [33].  $\text{CeO}_2$  has also successfully been employed in water splitting for  $\text{H}_2$  production and phenol and chlorinated phenol photodegradation under UV illumination [34]. Although photocatalytic activity of  $\text{CeO}_2$  has intensively been investigated, the broad band gap energy and the electronic potential position in the conductance and valence bands of this material seriously limit its further application as a photocatalyst utilizing solar energy [35]. Various strategies in liquid-phase system have been adopted for size-controlled synthesis of various functional nanomaterials, including transition metals doping [36], noble metals deposition [37], doping non-metallic elements [13], doping transition metals surface photosensitization [14] and coupled polycrystallites or colloidal semiconductors [15]. Thus, improving photocatalytic activity by coupled semiconductor has become hot topic among researchers.

Coupling of two semiconductors with different band gap level energies has been investigated extensively in the last decade as one of the most effective ways to decrease the frequency of the recombination of electron-hole ( $e^-/h^+$ ) pairs [16]. Many coupled semiconductors systems, such as  $\text{CeO}_2/\text{Fe}_2\text{O}_3$  [17],  $\text{CeO}_2/\text{ZnO}$  [18],  $\text{CeO}_2/\text{CeLnO}_x$  ( $\text{Ln} = \text{Pr}, \text{Tb}, \text{Lu}$ ) [19],  $\text{CeO}_2/\text{TiO}_2$  [20],  $\text{CeO}_2/\text{ZrO}_2$  [21],  $\text{CeO}_2/\text{MnO}_x$  [22],  $\text{CeO}_2/\text{Bi}_2\text{O}_3$  [23],  $\text{H}_3\text{PW}_{12}\text{O}_{40}\text{-CeO}_2/\text{TiO}_2$  and  $\text{CeO}_2/\text{TiO}_2$  [20],  $\text{CeO}_2/\text{CrO}$  [25],  $\text{CeO}_2/\text{MCM-41}$ ,  $\text{CeO}_2/\text{MCM-48}$  and  $\text{CeO}_2/\text{SBA-15}$  [26],  $\text{CeO}_2/\text{SiO}_2$  [27],  $\text{CeO}_2/\text{SrTiO}_3$  [28],  $\text{CeO}_2/\text{Ag-AgCl}$  [29],  $\text{CeO}_2/\text{BiVO}_4$  [30],  $\text{CeO}_2, \text{La}_2\text{O}_3, \text{C}/\text{TiO}_2$  [31],  $\text{CeO}_2/\text{Co}$  [32], have exhibited high photocatalytic efficiency owing to the improved charge separation and increased charge carrier lifetime.

In the present study, we have synthesized  $\text{CuBi}_2\text{O}_4/\text{CeO}_2$  nanocomposite photocatalysts by solid state route. The as-prepared  $\text{CuBi}_2\text{O}_4/\text{CeO}_2$  nanocomposites were characterized by X-ray diffraction (XRD), scanning electron microscopy (SEM) and UV-vis diffuse reflectance spectroscopy (DRS). The

photocatalytic efficiency of the samples was assessed by the degradation of Congo red (CR) dye, as probe reaction, under UVA light. Effects of the amount of added  $\text{CuBi}_2\text{O}_4$ , UV light and catalysts were investigated. The experimental data were quantified by applying the pseudo-first order kinetic model. The mechanisms of the increase in the photocatalytic activity were also discussed through the heterojunction charge modele.

## 2-EXPERIMENTAL

### 2-1-Materials and methods

#### 2-2-Materials

$\alpha\text{-Bi}_2\text{O}_3$  (99.99 %),  $\text{CuO}$  (99.99 %) and  $\text{CeO}_2$  (99.99 %) materials were obtained from Aldrich chemical company ltd. Congo red azoic dye (C.I. 22020,  $\text{MW} = 696.67 \text{ g mol}^{-1}$ ,  $\text{C}_{32}\text{H}_{24}\text{N}_6\text{O}_6\text{S}_2.2\text{Na}$ ,  $\lambda_{\text{max}} = 497 \text{ nm}$  and  $\text{pKa} = 4$ ) and other chemicals used in the experiments ( $\text{NH}_4\text{OH}$  and  $\text{H}_2\text{SO}_4$ ) were purchased from C.I.S.A Espagne.

#### 2-3-Preparation of p-CuBi<sub>2</sub>O<sub>4</sub>

The p- $\text{CuBi}_2\text{O}_4$  powder was prepared according to the previously reported procedure [38]. The stoichiometric proportion mixture of  $\alpha\text{-Bi}_2\text{O}_3$  and  $\text{CuO}$  oxides was previously ground for a period of time in an agate mortar, and then heated at the rate of  $5^\circ\text{C}/\text{min}$  in a muffle oven (Linn High Therm) and thermally treated at  $750^\circ\text{C}$  for 72 h in air. After the muffle oven was naturally cooled to room temperature, the black  $\text{CuBi}_2\text{O}_4$  powder was ground in the agate mortar and then was collected as the precursor to prepare the  $\text{CuBi}_2\text{O}_4/\text{CeO}_2$  photocatalysts.

#### 2-4-Preparation of CuBi<sub>2</sub>O<sub>4</sub>/CeO<sub>2</sub> photocatalyst

$\text{CuBi}_2\text{O}_4/\text{CeO}_2$  nanocomposite photocatalysts were prepared by the solid state technique with the  $\text{CuBi}_2\text{O}_4:\text{CeO}_2$  mass ratio of 5 : 95, 10 : 90, 20 : 80, 30 : 70, 40 : 60 and 50:50. The corresponding precursors of  $\text{CuBi}_2\text{O}_4/\text{CeO}_2$  were milled in an agate mortar for 30 minutes to form the nanosized photocatalysts.

#### 2-5-Characterization

X-ray diffraction patterns of the powders were recorded at room temperature using an automatic D8 Bruker AXS diffractometer with  $\text{CuK}\alpha$  radiation ( $\lambda = 1.5406 \text{ \AA}$ ) over the  $2\theta$  collection interval of  $10\text{-}70^\circ$  with a scan speed of  $10^\circ/\text{min}$ . The mean grain size ( $d_{\text{DRX}}$ ) was assessed using the Debye-Scherrer equation [39], as follows Eq. (1):

$$d_{\text{DRX}} = \frac{0.9 \lambda}{\beta \sin \theta} \quad [1]$$

where  $D$  is the mean grain size (nm),  $\lambda$  is the wavelength (nm),  $\beta$  is the corrected full width at half maximum (radian) and  $\theta$  is the Bragg angle (radian).

Where  $\beta$  is the corrected full-width at half maximum (FWHM) (radian),  $\lambda$  is the X-ray wavelength (1.5406 Å) and  $\theta$  is the Bragg angle (radian). The lattice constants of the samples calculated from their corresponding XRD pattern data are obtained by Fullprof program. UV-Vis DRS measurements were carried out at room temperature using a Perckin Elmer Lambda 650 spectrophotometer equipped with an integrating sphere attachment. The analysis range was from 200 to 900 nm, and polytetrafluoroethylene (PTFE, Teflon) was used as a reflectance standard. The band gap values were estimated by extrapolation of the linear part of the plot of absorbance versus the wavelength and  $E_g = 1240/\lambda_{\text{Absorp. Edge}}$  equation assuming that all the prepared photocatalysts are direct crystalline semiconductors. Scanning electron microscopy observations (SEM) were performed by using Hitachi S-4800N.

## 2-6-Photocatalytic study measurements

The photodegradation of CR catalyzed by the  $\text{CuBi}_2\text{O}_4/\text{CeO}_2$  samples was investigated under UV-light irradiation. 100 mg of catalyst was suspended in an CR solution (200 mL, 20 mg/L) in quartz cell tube. The suspension pH value was previous adjusted at 7 using NaOH/  $\text{H}_2\text{SO}_4$  solutions using (Hanna HI 210) pH meter. Prior to UV light irradiation, the suspension was stirred with magnetic stirrer (Speedsafe™ Hanna) for 30 min under dark at 25 °C to ensure the establishment of adsorption/desorption equilibrium between the catalyst and CR. The sample was then irradiated at 298 K using 6 W ultraviolet ( $\lambda=365$  nm, BLX-E365) photoreactor under continuous stirring. As the reaction proceeded, a 5 ml suspension was taken at 20 min intervals during the catalytic reaction and was centrifuged using centrifuge (EBA-Hetlich) at 3500 rpm for 15 min to completely remove photocatalyst particles. The residual RC concentrations during de course of degradation were monitored with UV mini-1240 Spectrophotometer (Shimadzu UV mini-1240) in the range 200 - 800 nm, using 1 cm optical pathway cells.

The effect of initial pH on the photocatalytic degradation of CR only conducted from pH 6 to 12 for avoiding dye aggregation. The experiments were also performed by varying the amount of  $\text{CuBi}_2\text{O}_4$  from 0 to 100 wt %. The data obtained from the photocatalytic degradation experiments were then used to calculate the degradation efficiency  $\eta'$  (%) of the substrate Eq. (2):

$$\eta'(\%) = \left[ \frac{C_i - C_f}{C_i} \right] 100 \quad [2]$$

where  $C_i$  dye initial concentration ( $\text{mg}\cdot\text{L}^{-1}$ ) and  $C_f$ : dye residual concentration after certain intervals ( $\text{mg}\cdot\text{L}^{-1}$ ).

According to the Planck's Law and some further calculation, we can find that the absorption wavelength of the photoreactor can be done by determining its' band gap value Eq. (3):

$$E_g = \frac{1239 \text{ eV}\cdot\text{nm}}{\lambda} \quad [3]$$

where  $h$  is Planck's constant ( $4.13566733 \cdot 10^{-15}$  eV. s);  $c$  is the speed of light ( $2.99792458 \cdot 10^{17}$  nm/s) and  $\lambda$  is the UVA- light wavelength (355-375 nm). From the calculation, in order to absorb a UVA-light wavelength, the band gap value of the photoreactor has to be below 3.49 eV and above 3.30 eV.

The photocatalytic degradation efficiency of catalyst for the degradation CR was quantified by measurement of dye apparent first order rate constants under operating parameters. Surface catalyzed reactions can often be adequately described by a monomolecular Langmuir-Hinshelwood mechanism, in which an adsorbed substrate with fractional surface coverage  $\theta$  is consumed at an initial rate given as follow Eq. (4) [40]:

$$-\left[ \frac{dC}{dt} \right] = r_0 = K_{\text{app}} \theta = \frac{K_1 K_2 C_0}{1 + K_1 C_0} \quad [4]$$

where  $K_1$  is a specific rate constant that changes with photocatalytic activity,  $K_2$  the adsorption equilibrium constant, and  $C_0$  is the initial concentration of the substrate. Inversion of the above rate equation is given by Eq. (5):

$$\frac{1}{K_{\text{app}} C_0} = \frac{1}{K_1 K_2} + \frac{C_0}{K_1} \quad [5]$$

Thus, a plot of reciprocal of the apparent first order rate constant  $1/K_{\text{app}}$  against initial concentration of the dye  $C_0$  should be a straight line with a slope of  $1/K_1$  and an intercept of  $1/K_1 K_2$ . Such analysis allows one to quantify the photocatalytic activity of catalyst through the specific rate constant  $K_1$  (with larger  $K_1$  values corresponding to higher photocatalytic activity) and adsorption equilibrium constant  $K_2$  ( $K_2$  expresses the equilibrium constant for fast adsorption-desorption processes between surface of catalyst and substrates). The integrated form of the above equation (Eq. 5) yields to the following Eq. (6):

$$t = \frac{1}{K_1 K_2} \ln \frac{C_0}{C} + \frac{1}{K_2} (C_0 - C) \quad [6]$$

where  $t$  is the time in minutes required for the initial concentration of the dye  $C_0$  to decrease to  $C$ . Since the dye concentration is very low, the second term of the expression becomes small when compared with the first one and under these conditions the above equation reduces to Eq. (7).

$$\ln \frac{C_0}{C} \approx K_1 K_2 t = K_{\text{app}} t \quad [7]$$

where  $k_{app}$  is the apparent pseudo-first order rate constant,  $C$  and  $C_0$  are the concentration at time 't' and 't=0', respectively. The plot of  $\ln C_0/C$  against irradiation time  $t$  should give straight lines, whose slope is equal to  $K_{app}$ .

The half-life of dye degradation at various process parameters was raised from Eq. (8).

$$t_{1/2} = \frac{0.5C_0}{K_2} + \frac{0.693}{K_1K_2} \quad [8]$$

Where half-life time,  $t_{1/2}$ , is defined as the amount of time required for the photocatalytic degradation of 50 % of CR dye in a aqueous solution by catalyst.

### 3-RESULTS AND DISCUSSIONS

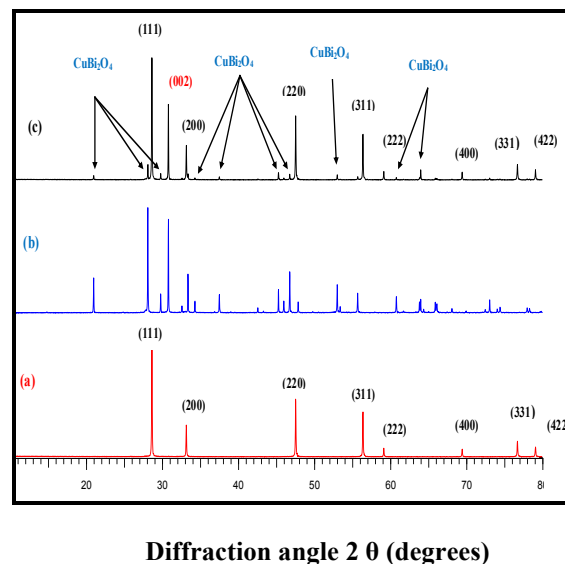
#### 3-1-XRD Analysis of (x wt%)CuBi<sub>2</sub>O<sub>4</sub>/CeO<sub>2</sub> composites

Figure 1 shows the XRD patterns of the as-synthesized (30 wt %) CuBi<sub>2</sub>O<sub>4</sub>/CeO<sub>2</sub> nanocomposites in comparison with those of CuBi<sub>2</sub>O<sub>4</sub> precursor and pure CeO<sub>2</sub>. Diffraction peaks of pure CeO<sub>2</sub> (Fig. 1a) at  $2\theta$  of 28.02°, 33.11°, 47.45°, and 56.3° can be indexed as the (111), (200), (220), and (311) planes of pure fluorite phase CeO<sub>2</sub>, which is in good agreement with standard value (Fm.3m, JCPDS file no. 34–0394) with lattice constant  $a=5.4110$  (2) Å. This is in agreement with the reported previous work [41]. The diffraction peaks of the Cubi<sub>2</sub>O<sub>4</sub> precursor (Fig. 1b) at  $2\theta$  of 28.03°, 29.73°, 30.73°, 32.54°, 33.36° and 46.7° were respectively indexed as (211), (220), (002), (102), (310), and (411) planes of pure tetragonal phase of crystalline Cubi<sub>2</sub>O<sub>4</sub>, according to the Joint Committee Powder Diffraction Standards (P4<sub>2</sub>/mnm, JCPDS file no. 42-0334) with lattice constants ( $a = 8.5004\text{Å}$ ,  $c = 5.819\text{Å}$ ) calculated from their corresponding XRD pattern data are obtained by Fullprof program. Both precursor CuBi<sub>2</sub>O<sub>4</sub> and pure CeO<sub>2</sub> show preferred (002) crystallographic orientation owing to the preparation route of the sample during the XRD analysis. The crystallite sizes of pure CeO<sub>2</sub> deduced from the XRD patterns by calculation of the Scherrer equation showed that crystalline size of the composite,  $d_{XRD}$  was calculated to 100 nm.

On the other hand, the XRD patterns of (30wt %) CuBi<sub>2</sub>O<sub>4</sub>/CeO<sub>2</sub> nanocomposites exhibited characteristic diffraction peaks of both Cubi<sub>2</sub>O<sub>4</sub> and CeO<sub>2</sub> crystalline phases. It can be seen from Fig.1c that at 30 % mass concentration of Cubi<sub>2</sub>O<sub>4</sub>, the diffraction pattern of the materials was quite similar to that of pure CeO<sub>2</sub>. This is probably due to the high crystallinity of the CeO<sub>2</sub> phase, thus appearing as the dominant peaks in the XRD spectra of the nanocomposite sample. Here, we observe that the XRD patterns (Figure 2) in the  $2\theta$

Thus the presence Cubi<sub>2</sub>O<sub>4</sub> promotes the crystallinity and a consequent broadening of the diffraction peaks of the (30 wt %) CuBi<sub>2</sub>O<sub>4</sub>/CeO<sub>2</sub> nanocomposites

range from 25° to 40° show that (30 wt %) CuBi<sub>2</sub>O<sub>4</sub>/CeO<sub>2</sub> nanocomposites sample exhibits broadened peaks with a little shift toward higher intensities. Based on the Scherrer equation, the crystallite size of a sample is inversely proportional to the full-width-half-maximum (FWHM), indicating that a broader peak represents smaller crystallite size [42].



**Figure 1** XRD patterns of pure CeO<sub>2</sub> (a) precursor CuBi<sub>2</sub>O<sub>4</sub> (b) and the synthesis (30 wt %) CuBi<sub>2</sub>O<sub>4</sub>/CeO<sub>2</sub> (c).

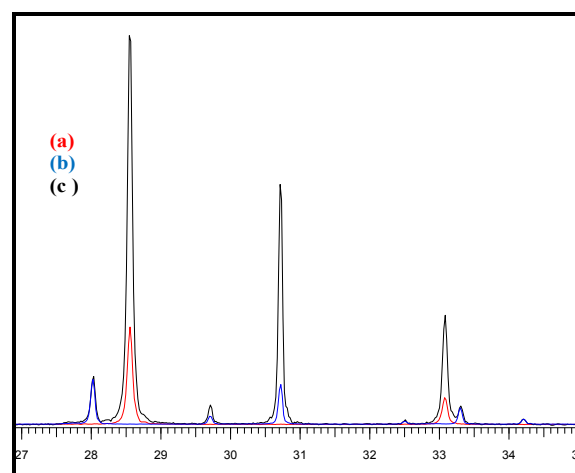


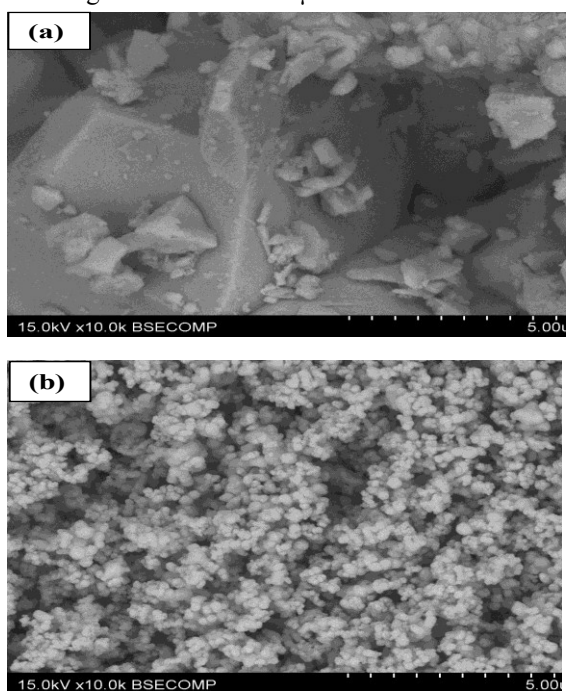
**Figure 2** XRD patterns of pure CeO<sub>2</sub> (a) precursor CuBi<sub>2</sub>O<sub>4</sub> (b) and the synthesized (30 wt %) CuBi<sub>2</sub>O<sub>4</sub>/CeO<sub>2</sub> (c), in the  $2\theta$  range from 25° to 40°.

#### SEM analysis

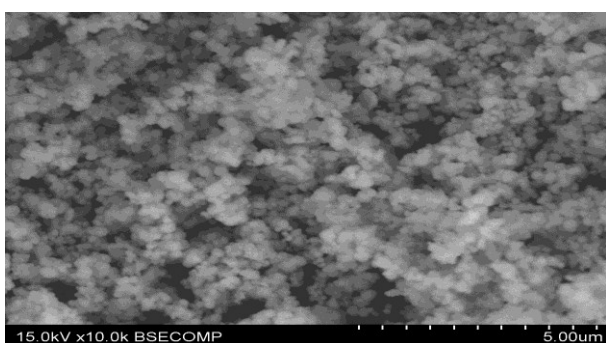
Figure 3 illustrates typical SEM images of CuBi<sub>2</sub>O<sub>4</sub> powder synthesized by solid-state reaction of CuO and  $\alpha$ -Bi<sub>2</sub>O<sub>3</sub> at 750 °C for 24 h (figure 3a) and pure CeO<sub>2</sub> (figure 3b) shows typical high-resolution SEM

image of  $\text{CuBi}_2\text{O}_4$  powder. As shown in figure 3a, it clearly shows two different crystal shapes on the  $\text{CuBi}_2\text{O}_4$  surface, corresponding to two different particle sizes of  $\text{CuBi}_2\text{O}_4$ . The appearance of  $\text{CuBi}_2\text{O}_4$  is a shape sheet and a well-defined tetragonal phase with the crystallite diameter of the  $\text{CuBi}_2\text{O}_4$  is about  $5\mu\text{m}$ , where as groups of smaller particles do not have any specific

shape with size up to 500 nm tend to cover the bigger particles. However, pure  $\text{CeO}_2$  from SEM analysis (figure 3b) clearly shows two different spherical-shaped nanoparticles structures on the  $\text{CeO}_2$  surface, which can be assigned to  $\text{CeO}_2$  with a particle size in the range of 100 nm and  $\text{Ce}_2\text{O}_3$  with approximately 200 nm dimensions, which agrees with the UV-Vis diffuse reflectance of Ceria. Both nanoparticles are close to each other in the form of chains. The as synthesized (30 wt%) $\text{CuBi}_2\text{O}_4/\text{CeO}_2$  nanocomposite (figure 4) clearly shows the presence of  $\text{CeO}_2$  nanoparticles deposited onto the  $\text{CuBi}_2\text{O}_4$  surface, displaying a particle size of 100-200 nm and strong assembly of the nanoparticles measuring from 200 nm to 1  $\mu\text{m}$ . surface area.



**Figure 3** SEM images of (a) high-resolution of precursor  $\text{CuBi}_2\text{O}_4$  (b) pure  $\text{CeO}_2$



**Figure 4** SEM image of (30 wt %)  $\text{CuBi}_2\text{O}_4/\text{CeO}_2$  nanocomposite.

### 3-2-UV-Vis Diffuse Reflectance Spectra and Band Gap Energy.

Figures 5 and 6 show the UV-vis absorbance spectra of  $\text{CuBi}_2\text{O}_4$  and pure  $\text{CeO}_2$  respectively. It is clear from the recorded UV-visible spectrum of  $\text{CeO}_2$  that two absorption bands are observed in the UV region at 345 and 245 nm. Generally, the absorption of ceria in the UV region originates from the charge-transfer transition between the O 2p and Ce 4f states in  $\text{O}^{2-}$  and  $\text{Ce}^{4+}$ . This spectral profile indicates that charge-transfer transition of  $\text{Ce}^{4+}$  overlaps with the  $4f^1 \rightarrow 5d^1$  transition of  $\text{Ce}^{3+}$  [43]. It can be seen from figure 5, that it has strong and broad absorption in the range of 200–900 nm. This suggests that the prepared sample absorb both UV and visible light. Obviously, for  $\text{CuBi}_2\text{O}_4$  nanostructures, the broad absorption band observed in the UV-visible region was attributed to the charge-transfer transition between the O 2p and Cu  $3dx^2-y^2$  states in  $\text{O}^{2-}$  and  $\text{Cu}^{2+}$  respectively [44].

Figure 6 shows UV-Vis DR spectra of a series of photocatalysts (x wt %)  $\text{CuBi}_2\text{O}_4/\text{CeO}_2$ . It can be seen that the absorption wavelength range of the (x wt %)  $\text{CuBi}_2\text{O}_4/\text{CeO}_2$  is extended greatly toward visible light and its absorption intensity is also increased in comparison with pure  $\text{CeO}_2$ . The red-shift observed in the  $\text{CeO}_2$  would be explained by the formation of localized states within the band gap owing to oxygen vacancies and increase  $\text{Ce}^{3+}$  ion concentration. This phenomenon is due to the shift of absorbance band shift towards the longer wavelength [45].

The onset absorption edges and band gap energies of  $\text{CuBi}_2\text{O}_4$ ,  $\text{CeO}_2$  and (x wt %)  $\text{CuBi}_2\text{O}_4/\text{CeO}_2$  samples are shown in figures 5 and 6 respectively. The as-synthesized  $\text{CuBi}_2\text{O}_4$  exhibits an absorption onset at 900 nm, which correspond to band gap energy of 1.38 eV. It is clear from the recorded spectrum, that  $\text{CeO}_2$  nanocrystalline has two absorption onsets at 390 and 520 nm, which match to band gap energies of 3.18 and 2.38 eV, attributing to  $\text{CeO}_2$  dioxide and  $\text{Ce}_2\text{O}_3$  sesquioxide respectively. These results are in well agreement with values reported in the literature [46, 47]. The optical properties of the as-synthesized  $\text{CuBi}_2\text{O}_4$  and pure  $\text{CeO}_2$  nanoparticles are reported in table 1

It is widely accepted that electronic transport properties depend on the physical and structural characteristics of photocatalyst, such as crystallite size, morphology, phase structure and amount of  $\text{CuBi}_2\text{O}_4$  loaded. As reported from the UV-vis DRS in Figure 7 and table 2, for the series of (x wt %)  $\text{CuBi}_2\text{O}_4/\text{CeO}_2$  nanocomposites, the band gap energy decreased from 3.18 to 3.12 eV as the amount of  $\text{CuBi}_2\text{O}_4$  was increased up to 40 % on the  $\text{CeO}_2$  matrix, suggesting that the physical preparation of nanocomposite powders will

result in good particle-to-particle connections, especially in cases where a high electrical conductivity [48]. So, the decrease of the band gap energy with an enhanced absorption intensity of the (30 wt %) CuBi<sub>2</sub>O<sub>4</sub>/CeO<sub>2</sub> nanocomposites upon loading the amount of CuBi<sub>2</sub>O<sub>4</sub> could be ascribed to the homogeneous dispersion of CuBi<sub>2</sub>O<sub>4</sub> within the CeO<sub>2</sub> matrix in the bulk of the catalyst and the formation of conducting network at very low temperature.

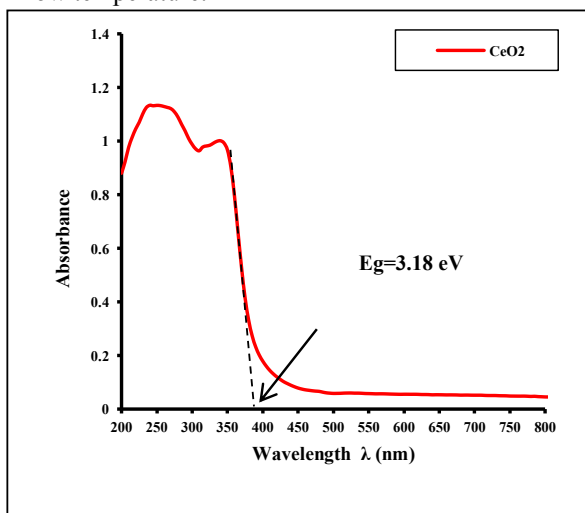


Figure 5 UV-visible absorbance spectra of pure C

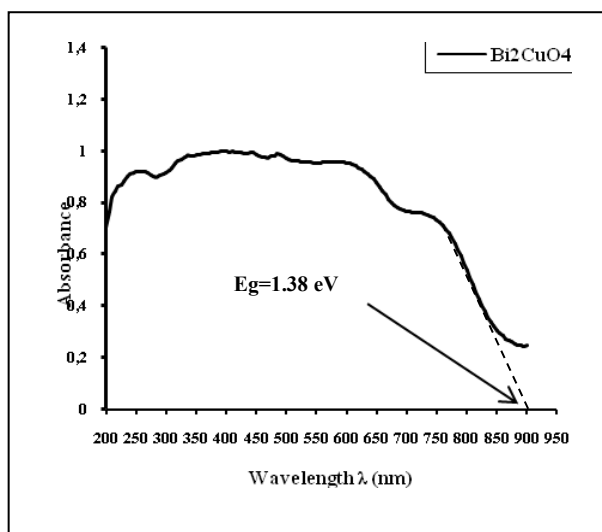


Figure 6 UV-visible absorbance spectra of CuBi<sub>2</sub>O<sub>4</sub> synthesized by solid-state reaction at 750 °C for 24 h

Table 1 Optical properties of the as-synthesized CuBi<sub>2</sub>O<sub>4</sub> and pure CeO<sub>2</sub> nanoparticles

Systems	λ (nm)	Charge-transfer transition	Band gap Eg (eV)	
			Experimental	Literature Ref.
CuBi <sub>2</sub> O <sub>4</sub>	900	$2 p^6 (O) \rightarrow 3 dx^2-y^2 (Cu)$	1.38	1.5
CeO <sub>2</sub>	390	$2 p^6 (O) \rightarrow 4 f^0 (Ce)$	3.18	2.7-3.4

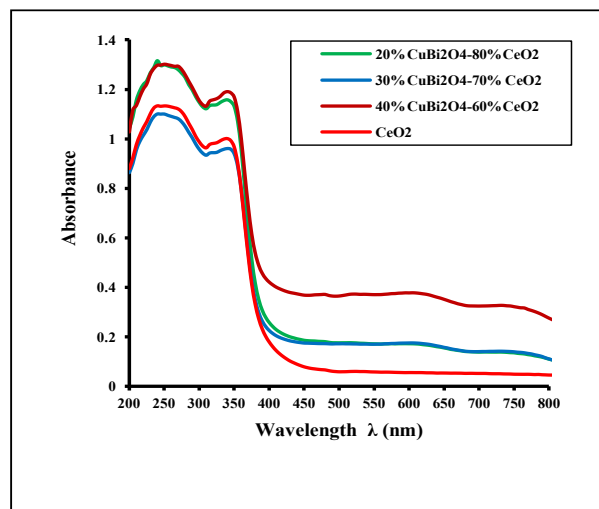


Figure 7 UV-visible absorbance spectra of a series of (x wt %) CuBi<sub>2</sub>O<sub>4</sub>/CeO<sub>2</sub> nanocomposites

**Table 2** Optical properties of a series of (x wt %)  $\text{CuBi}_2\text{O}_4/\text{CeO}_2$  composites

Amount of $\text{CuBi}_2\text{O}_4$ (%)	Charge-transfer transition $2p^6(\text{O}) \rightarrow 4f^0(\text{Ce})$		Charge-transfer transition $4f^0(\text{Ce}) \rightarrow 4f^1(\text{Ce})$	
	$\lambda$ (nm)	Band gap $E_g$ (eV)	$\lambda$ (nm)	Band gap $E_g$ (eV)
0	390	3.18	520	2.38
20	390	3.18	495	2.51
30	395	3.14	500	2.48
40	397	3.12	490	2.53

### 3-3-Photocatalytic activity tests

#### 3-3-1. Effect of the amount of $\text{CuBi}_2\text{O}_4$ on the photocatalytic activity of (x wt %) $\text{CuBi}_2\text{O}_4/\text{CeO}_2$

The effect of the amount of  $\text{CuBi}_2\text{O}_4$  on photocatalytic degradation of CR was conducted over a range of catalyst amount from  $x = 0$  to  $x = 100$  wt %. As observed in figure 8, it is evident that the photocatalytic redox of CR greatly depends on the amount of doped  $\text{CuBi}_2\text{O}_4$ . The photocatalytic activity increased drastically from 14.928 % to 83.054 % as the catalyst amount was raised from  $x = 0$  to  $x = 30$  wt %. Further increase in the  $\text{CuBi}_2\text{O}_4$  amount beyond of  $x = 30$  wt %, the photocatalytic activity decreased gradually, almost reaching 3.13 % at  $x = 100$  wt %. The maximum photocatalytic activity of (x wt %)  $\text{CuBi}_2\text{O}_4/\text{CeO}_2$  (83.054 %) under UVA- light irradiation was achieved within 100 min of light illumination time when the amount of doped  $\text{CuBi}_2\text{O}_4$   $x$  was 30 wt %. So there is an optimum  $\text{CuBi}_2\text{O}_4$  contents for high dispersion morphology of nanoparticles  $\text{CuBi}_2\text{O}_4$  on the  $\text{CeO}_2$  surface with high activity.

The effective electron-hole separation both at the physically bonded interfaces and in the two semiconductors as well as charge defect during the physical mixing method was believed to be mainly responsible for the remarkably enhanced photocatalytic activity of (30 wt %)  $\text{CuBi}_2\text{O}_4/\text{CeO}_2$  in the course of the photocatalytic redox conversion of CR.

But until now, there are no reports about synergistic effect between  $\text{CeO}_2$  and  $\text{CuBi}_2\text{O}_4$  in the (30 wt %)  $\text{CuBi}_2\text{O}_4/\text{CeO}_2$  composite under visible light excitation. From figure 8, it is clear that the photocatalytic activity of  $\text{CeO}_2$  is drastically increased under the presence of an amount of  $\text{CuBi}_2\text{O}_4$  (30 wt %) compared to pure  $\text{CeO}_2$  and the  $\text{CuBi}_2\text{O}_4$  samples. These results strongly suggest the existence of a synergistic effect between  $\text{CeO}_2$  and the  $\text{CuBi}_2\text{O}_4$  in the (30 wt %)  $\text{CuBi}_2\text{O}_4/\text{CeO}_2$  composite under UVA light excitation.

However, at higher amount of doped  $\text{CuBi}_2\text{O}_4$  than 30 wt %, the photocatalytic redox activity of (x wt%)  $\text{CuBi}_2\text{O}_4/\text{CeO}_2$  photocatalyst was obviously decreased on further increase in amount of  $\text{CuBi}_2\text{O}_4$ . Thus, such an above occurrence in the present experiment is primarily attributed to overlapping of adsorption sites of  $\text{CeO}_2$  particles as a result of overcrowding of the  $\text{CuBi}_2\text{O}_4$  granule owing to the decrease in screening effect and interfering of light. An analogous trend was reported in the reduction of  $\text{Cr}_2\text{O}_7^{2-}$  and photocatalytic oxidation of methylene blue orange (MB) using p-n heterojunction photocatalyst  $\text{CuBi}_2\text{O}_4/\text{Bi}_2\text{WO}_6$  [49].

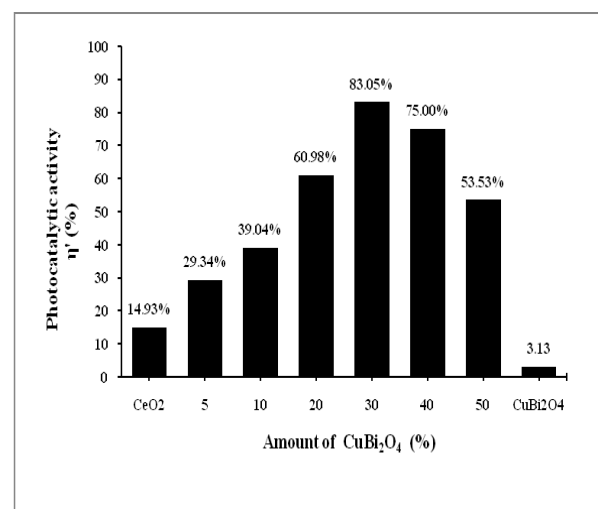


**Figure 8** Effect of the amount of  $\text{CuBi}_2\text{O}_4$  on the photocatalytic redox of CR under UV light irradiation ( [Catalyst] = 0.5 g/L, [CR]= 20 mg/L, pH = 7, T = 298 K,  $\lambda_{\text{max}} = 365$  nm, I = 90 J /cm<sup>2</sup> and irradiation time = 100 min).

#### 3-3-2. Effect of UV light and catalyst

The photocatalytic activities of all three  $\text{CuBi}_2\text{O}_4$ ,  $\text{CeO}_2$ , (30 wt %)  $\text{CuBi}_2\text{O}_4/\text{CeO}_2$  photocatalysts were assessed by the photocatalytic redox reaction of Congo red (CR) aqueous solution under UVA-light irradiation. Variations of CR reduced concentration ( $C/C_0$ ) versus visible-light irradiation

time (t) over different catalysts under different experimental conditions through UV-A alone, UVA/CuBi<sub>2</sub>O<sub>4</sub>, UVA/CeO<sub>2</sub>, (30 wt %) CuBi<sub>2</sub>O<sub>4</sub>/CeO<sub>2</sub> and UVA/(30 wt %) CuBi<sub>2</sub>O<sub>4</sub>/CeO<sub>2</sub> are presented in figure 8, Results showed that (30 wt %) CuBi<sub>2</sub>O<sub>4</sub>/CeO<sub>2</sub> exhibited higher photocatalytic performance, as compared to the single phases CuBi<sub>2</sub>O<sub>4</sub> and CeO<sub>2</sub>. The highest efficiency was obtained, under UV-light irradiation over (30 wt %) CuBi<sub>2</sub>O<sub>4</sub>/CeO<sub>2</sub>, as a result of 83.05 % degradation of CR for 100 min of irradiation time. However, the photocatalytic degradation of CR over single phases CuBi<sub>2</sub>O<sub>4</sub> and CeO<sub>2</sub> were only 3.13 and 14.92 % respectively. When 20 mg/L of CR along with (30 wt %)CuBi<sub>2</sub>O<sub>4</sub>/CeO<sub>2</sub> was magnetically stirred for the same optimum irradiation time in the absence of light, lower (21.48 %) degradation was observed, whereas, disappearance of dye was negligible (0.49 %) in the direct photolysis. On the basis of these results, the high decomposition of CR dye in the presence of (30 wt %) CuBi<sub>2</sub>O<sub>4</sub>/CeO<sub>2</sub> catalyst is exclusively attributed to the photocatalytic reaction of the combined semiconductor particles under UV light irradiation. Thus, such an above occurrence in the present experiment is primarily assigned to the charge defect during the physical mixing method, which is advantageous for the effective electron-hole separation and the suppression of the recombination rate of the photogenerated charge carriers.

### 3-3-3. Kinetic modelling

The photocatalytic degradation of CR over different experimental conditions was displayed in table 3. As it can be seen, the straight lines for the entire as-prepared samples of the plots of  $\ln C/C_0$  versus t with high regression coefficients ( $R^2 = 0.892-0.939$ ), for the pseudo-first-order kinetic model strongly suggest that all the photodegradation systems were a pseudo-first-order model. Exception was observed in the cases of photodegradation and adsorption reactions in the presence of the single phase CuBi<sub>2</sub>O<sub>4</sub> and the combined semiconductors respectively.

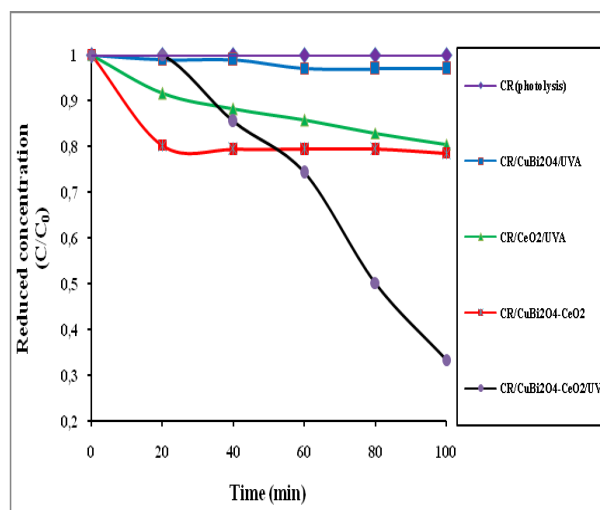


**Figure 9** Photocatalytic degradation kinetics of CR at different experimental conditions ([Catalyst] = 0.5 g/L, [CR] = 20 mg/L, pH = 7, T = 298 K,  $\lambda_{\max}$  = 365 nm, I=90 J/cm<sup>2</sup> and irradiation time = 100 min).

## 4-Discussion of mechanism

The above analysis shows that the migration direction of the photogenerated charge carrier depends on the band edge positions of the two semiconductors. There are three methods to determine the band edge positions: experiments based on photoelectrochemical techniques, calculation according to the first principle, and predicting theoretically from the absolute (or Mulliken) electronegativity [50-52]. The first one is not always easy to handle, and the second one cannot obtain the absolute energy of band edges with respect to vacuum and always has large discrepancies between calculated and measured values. The third one is a simple approach with reasonable results for many oxides photocatalysts [45].

The conduction band edge of a semiconductor at the point of zero charge (pH zpc) can be predicted by Eq. (14) :

$$E_{CB}^0 = \chi - E_C - 1/2E_g. \quad [14]$$

where  $\chi$  is the absolute electronegativity of the semiconductor ( $\chi$  is 5.56 eV and 4.75 eV for CeO<sub>2</sub> and CuBi<sub>2</sub>O<sub>4</sub>, respectively).  $E_C$  is the energy of free electrons on the hydrogen scale (4.5 eV) and  $E_g$  is the band gap of the semiconductor. The predicted band edge positions of CuBi<sub>2</sub>O<sub>4</sub>, CeO<sub>2</sub> and Ce<sub>2</sub>O<sub>3</sub> by the above equation are shown in table 4. Photocatalytic reaction proceeds owing to holes and electrons generated in materials by absorbing light energy. The photogenerated holes have oxidation ability and the photogenerated electrons have reduction ability. For decomposition of organic pollutants by photocatalytic reaction, the oxidation potential of hole needs to be more positive than + 1 V that is redox potential of

general organic compounds as well as of hydroxyl radical ( $E_0(\text{H}_2\text{O}/\cdot\text{OH}) = 2.8 \text{ V/NHE}$ ). In addition, the redox potential of electrons needs to be more negative than that of superoxide radical ( $E_0(\text{O}_2/\text{O}_2^{\cdot-}) = -0.28 \text{ V/NHE}$ ).

The as-prepared CuBi<sub>2</sub>O<sub>4</sub> is a p-type semiconductor, which always exhibits good stability under UV-visible illumination, and CeO<sub>2</sub> is determined as an n-type material. Figure 10 and 11 depict reaction schemes of CuBi<sub>2</sub>O<sub>4</sub> and CeO<sub>2</sub> as the p and n an type respectively for charge separation for the reductivity/oxidizability improvement model. According to Figure 14, when the CuBi<sub>2</sub>O<sub>4</sub> and CeO<sub>2</sub> photocatalysts are irradiated under UVA (365 nm) light, both catalysts CuBi<sub>2</sub>O<sub>4</sub> and CeO<sub>2</sub> can be activated since the band gap energies of CuBi<sub>2</sub>O<sub>4</sub> observed in this study were 3.18 and 1.38 eV respectively.

For the p-CuBi<sub>2</sub>O<sub>4</sub> (figure 10), the electronic potential of the conduction band bottom of p-CuBi<sub>2</sub>O<sub>4</sub> is around  $-0.44 \text{ eV/NHE}$  which is more negative than that of superoxide radical ( $E_0(\text{O}_2/\text{O}_2^{\cdot-}) = -0.28 \text{ V/NHE}$ ). This indicated that the electron photoproduced at the conduction band directly reduced O<sub>2</sub> into O<sub>2</sub><sup>·-</sup>. These reduced O<sub>2</sub><sup>·-</sup> can subsequently transfer the charge to the species present in the reaction medium that are preferentially adsorbed onto the p-CuBi<sub>2</sub>O<sub>4</sub> particles. Hence, the superoxide radical (O<sub>2</sub><sup>·-</sup>) reduce the recombination of the charge carriers enhancing the activity in the UVA light. However, the p-CuBi<sub>2</sub>O<sub>4</sub> valence band top of  $+0.94 \text{ eV/NHE}$ , which is too negative than that of hydroxyl radical ( $E_0(\text{H}_2\text{O}/\cdot\text{OH}) = +2.8 \text{ V/NHE}$ ). The holes photogenerated in the p-CuBi<sub>2</sub>O<sub>4</sub> are not able to oxidize H<sub>2</sub>O to  $\cdot\text{OH}$ . But it is approximately enough to decompose organic pollutants. The presence of non stoichiometric regions of the nominally p-CuBi<sub>2</sub>O<sub>4</sub> particles or small domains of binary oxide phases of Cu<sub>x</sub>O or Bi<sub>x</sub>O, undetected by XRD data, as unstable impurity phases which could be originated from a number of processes such as reduction of the p-CuBi<sub>2</sub>O<sub>4</sub>, could be responsible for higher recombination rates [43].

On the other hand, pure CeO<sub>2</sub> (figure 11) shows little photocatalytic activity under UVA light. Since the top of the valence band of CeO<sub>2</sub> is around  $+2.65 \text{ eV/NHE}$  and the bottom of the conduction band of CeO<sub>2</sub> is around  $-0.53 \text{ eV/NHE}$ , we expect that photogenerated electrons at the conduction band of CeO<sub>2</sub> can directly reduced O<sub>2</sub> into O<sub>2</sub><sup>·-</sup> because electronic potential of the conduction band bottom of CeO<sub>2</sub> ( $-0.53 \text{ V/NHE}$ ) which is more negative than that of superoxide radical ( $E_0(\text{O}_2/\text{O}_2^{\cdot-}) = -0.28 \text{ V vs. NHE at pH 7}$ ). In contrast, the CeO<sub>2</sub> valence band top of  $+2.65 \text{ eV/NHE}$  is more anodic than that of hydroxyl radical ( $E_0(\text{H}_2\text{O}/\cdot\text{OH}) = +2.8 \text{ V/NHE}$ ), indicating that the photogenerated holes in the CeO<sub>2</sub> cannot oxidize H<sub>2</sub>O to  $\cdot\text{OH}$ . These reduced O<sub>2</sub><sup>·-</sup> species can subsequently transfer the charge to the present in the reaction

medium. Thus, the superoxide radical (O<sub>2</sub><sup>·-</sup>) suppress the recombination of the charge carriers enhancing the photocatalytic activity in the UVA light as well.

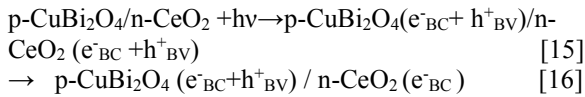
Moreover, the reduction of Ce<sup>+4</sup> to Ce<sup>+3</sup> requires a potential of  $+1.61 \text{ V/NHE}$  and oxidation of Ce<sup>+3</sup> to Ce<sup>+4</sup> requires  $-1.61 \text{ V/NHE}$ . The bottom of the conduction band of CeO<sub>2</sub> is around  $-0.53 \text{ eV/NHE}$ , is more anodic than that of Ce<sup>+4</sup> to Ce<sup>+3</sup> reduction potential. Hence, the photogenerated electrons at the conduction band of CeO<sub>2</sub> can directly reduced Ce<sup>+4</sup> to Ce<sup>+3</sup>. Also, the CeO<sub>2</sub> valence band top of  $+2.65 \text{ eV/NHE}$  is more positive than Ce<sup>+3</sup> to Ce<sup>+4</sup> oxidation potential. The photogenerated electrons at the valence band of CeO<sub>2</sub> can hence oxidize Ce<sup>+3</sup> to Ce<sup>+4</sup>. These reduced Ce<sup>+3</sup> and oxidized Ce<sup>+4</sup> species can In a contrast experiment, p-CuBi<sub>2</sub>O<sub>4</sub>/n-CeO<sub>2</sub> composite exhibits higher activity than phases p-CuBi<sub>2</sub>O<sub>4</sub> and n-CeO<sub>2</sub>. The possible reason for the remarkably enhanced photocatalytic performance of p-CuBi<sub>2</sub>O<sub>4</sub>/n-CeO<sub>2</sub> in the course of the photocatalytic redox of Congo red can be explained by p-n type heterojunction formation model of the electron-hole separation process under UV light irradiation. The schematic diagram p-n heterojunction formation model is depicted in figure 10.

with wavelengths below 900 nm, whereas n-CeO<sub>2</sub> with band gap of is about 3.18 eV can be excited by photons with wavelengths of 390 nm. So at the interfaces of p-CuBi<sub>2</sub>O<sub>4</sub> loaded n-CeO<sub>2</sub> composite, a p-n heterojunction would be formed.

According to the band edge position (table 1), the electronic potential of the conduction band bottom of n-CeO<sub>2</sub> is slightly more anodic than that of p-CuBi<sub>2</sub>O<sub>4</sub>, whereas, the hole potential of the valence band top of n-CeO<sub>2</sub>, which is more positive than that of p-CuBi<sub>2</sub>O<sub>4</sub>. Under UVA ( $\lambda_{\text{UVA}} = 355\text{-}375 \text{ nm} \rightarrow E_{\text{hv}} = 3.30\text{-}3.49 \text{ eV}$ ) light irradiation, the energy of the excitation light was large enough to yield an excited state of both p-CuBi<sub>2</sub>O<sub>4</sub> ( $\lambda_{\text{CuBi}_2\text{O}_4} = 900 \text{ nm} \rightarrow E_{\text{g}} = 1.38 \text{ eV}$ ) and n-CeO<sub>2</sub> ( $\lambda_{\text{CeO}_2} = 390 \text{ nm} \rightarrow E_{\text{g}} = 3.18 \text{ eV}$ ) semiconductors. A part of the photogenerated charge carriers, free electron (e<sup>-</sup>) and electronic vacancy-a hole (h<sup>+</sup>), recombines in the bulk of the semiconductors, while the rest transfer in the photocatalyst surfaces being partially localized on structural defective centers of its crystalline lattice.

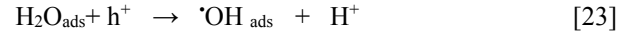
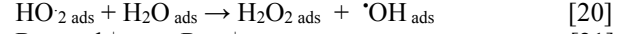
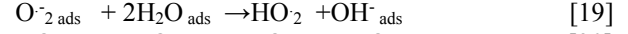
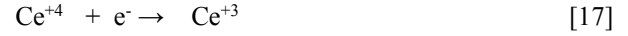
So, when p-type semiconductor CuBi<sub>2</sub>O<sub>4</sub> and n-type semiconductor CeO<sub>2</sub> were connected to each other, p-n heterojunction will be formed between p-CuBi<sub>2</sub>O<sub>4</sub> and n-CeO<sub>2</sub>, and at the equilibrium the inner electric field will be also produced at the same time in the interface. So a number of micro p-n heterojunction CuBi<sub>2</sub>O<sub>4</sub>/CeO<sub>2</sub> photocatalysts will be formed after doping p-CuBi<sub>2</sub>O<sub>4</sub> powder into n-CeO<sub>2</sub> granule. The electron-hole pairs will be created under UV light illumination. With the effect of the inner electric field, the holes can transfer from n-CeO<sub>2</sub> to p-CuBi<sub>2</sub>O<sub>4</sub>

easily, but the electrons cannot move from n-CeO<sub>2</sub> to p-CuBi<sub>2</sub>O<sub>4</sub>. If electrons transferred to p-CuBi<sub>2</sub>O<sub>4</sub>, the photocatalytic activity would decrease because of recombination. Although the transfer of electrons is feasible for the potential between the two conduction bands, it is blocked because of the inner electric field. So the minor carrier in n-CeO<sub>2</sub>, which is the control factor of recombination in this n-CeO<sub>2</sub> semi-conductor, can transfer out. In this way, the photoinduced electron (e<sup>-</sup>)-hole (h<sup>+</sup>) pairs in the two semiconductors were effectively separated by the p-n junction formed in the CuBi<sub>2</sub>O<sub>4</sub>/CeO<sub>2</sub> catalyst and transferred to the semiconductor/substrate interfaces efficiently, thus the probability of electron-hole recombination was reduced. As a result, a larger amount holes on p-CuBi<sub>2</sub>O<sub>4</sub> surface and a net effect of electrons on n-CeO<sub>2</sub> surface acting as powerful oxidants respectively Eq.(15-16). The stepwise photocatalytic mechanism is illustrated below:

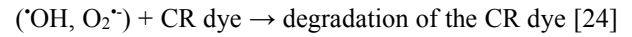


The photogenerated electrons as well as holes act as powerful oxidants, respectively. The photogenerated electrons at the conduction band of n-CeO<sub>2</sub> can directly reduced Ce<sup>+4</sup> to Ce<sup>+3</sup> Eq. (17) and react with the adsorbed molecular O<sub>2ads</sub> on the p-CuBi<sub>2</sub>O<sub>4</sub>/n-CeO<sub>2</sub> catalyst sites, reducing it to superoxide anion (O<sup>-</sup><sub>2ads</sub>), hydroperoxide (HO<sub>2ads</sub>) radicals and hydrogen peroxide (H<sub>2</sub>O<sub>2 ads</sub>) Eq. (18-20), while the photogenerated holes at the valance band of p-CuBi<sub>2</sub>O<sub>4</sub> can oxidize either the CR dye molecule directly Eq.(21) or both hydroxyl ions and water molecules adsorbed on the photocatalyst

surface forming the organic cation-radicals (R<sup>+</sup><sub>ads</sub>) Eq. (22), and hydroxylic radicals (HO<sup>•</sup><sub>ads</sub>) Eq. (23). These processes could be represented in the following equations:



The hydroxylic, peroxide and hydroperoxide radicals formed on the illuminated p-CuBi<sub>2</sub>O<sub>4</sub>/n-CeO<sub>2</sub> catalyst surface via either a photoexcitement of CeO<sub>2</sub> semiconductor and/or photosensibilization of CuBi<sub>2</sub>O<sub>4</sub> are highly effective oxidizing agent in the p-CuBi<sub>2</sub>O<sub>4</sub>/n-CeO<sub>2</sub> mediated photocatalytic oxidation of Congo red Eq. (24).



The primary reason for the observed maximum photocatalytic activity of the p-CuBi<sub>2</sub>O<sub>4</sub>/n-CeO<sub>2</sub> nanocomposites can be attributed to p-CuBi<sub>2</sub>O<sub>4</sub> being less active than n-CeO<sub>2</sub>. At 30wt% p-CuBi<sub>2</sub>O<sub>4</sub> loading, the amount of Ce<sup>+4</sup>/Ce<sup>+3</sup> present on the p-CuBi<sub>2</sub>O<sub>4</sub>/n-CeO<sub>2</sub> nanocomposites surface is favorable for faster charge transfer and at the same time allows light to reach the p-CuBi<sub>2</sub>O<sub>4</sub>/n-CeO<sub>2</sub> surface. Similar trend was reported in the efficient Photocatalytic Degradation of Phenol over Co<sub>3</sub>O<sub>4</sub>/BiVO<sub>4</sub> Composite under Visible Light Irradiation [53].

**Table 3** Kinetic parameters of photocatalytic degradation of CR on (30 wt%)CuBi<sub>2</sub>O<sub>4</sub>/CeO<sub>2</sub>, compared to the pure and combined catalysts systems ( [Catalyst] = 0.5 g/L, [CR] = 20 mg/L, pH = 7-8, T = 298 K, λ<sub>max</sub> = 365 nm, I = 90 J/cm<sup>2</sup> and irradiation time = 100 min).

Systems	η (%)	η' (%)	K <sub>1</sub> (min <sup>-1</sup> )	t <sub>1/2</sub> (min)	R <sup>2</sup> (%)
RC/UV-A	-	0.49	-	-	-
RC/(30 wt %) CuBi <sub>2</sub> O <sub>4</sub> -CeO <sub>2</sub>	21.48	-	-	-	-
RC/CeO <sub>2</sub> /UVA	8.00	14.92	0.0024	288.811	0.892
RC/(30 wt %) CuBi <sub>2</sub> O <sub>4</sub> -CeO <sub>2</sub> /UVA	17.30	83.05	0.0133	52.116	0.939
RC/CuBi <sub>2</sub> O <sub>4</sub> /UVA	0	3.13	0.0002	3465.736	0.203

**Table 4** Absolute electronegativity, estimated band gap, energy levels of calculated conduction band edge, and valence band at the point of zero charge for  $\text{CuBi}_2\text{O}_4$ ,  $\text{CeO}_2$  and  $\text{Ce}_2\text{O}_3$

Catalyst	$\chi$ (eV)	$\lambda$ (nm)	$E_g$ (eV)	$E_{BC}^0$ (eV)	$E_{BV}^0$ (eV)
$\text{CuBi}_2\text{O}_4$	4,75	900	1,38	-0.44	+0.94
$\text{CeO}_2$	5,56	390	3.18	-0.53	+2,65
$\text{Ce}_2\text{O}_3$	5,20	520	2.38	-0.49	+1.89

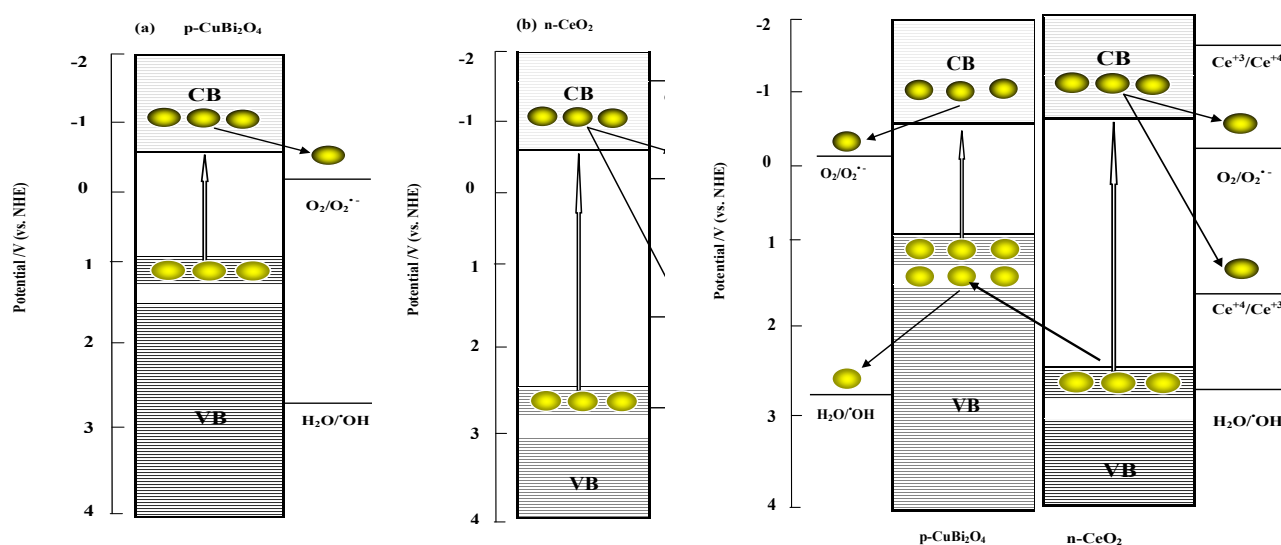


**Figure 10** Reaction schemes of  $\text{CuBi}_2\text{O}_4$  (a) and  $\text{CeO}_2$  (b) as the p and n an type respectively for charge separation for the reductivity/oxidizability improvement model (electron ● and hole ●).

**Figure 11** Reaction scheme of  $\text{CuBi}_2\text{O}_4/\text{CeO}_2$  as the p-n type charge separation for the reductivity/oxidizability improvement model (electron ● and hole ●).

## CONCLUSION

Novel  $\text{p-CuBi}_2\text{O}_4/\text{n-CeO}_2$  composite photocatalysts with different mass ratios were synthesized with the grinding–annealing method. The as-prepared  $\text{p-CuBi}_2\text{O}_4/\text{n-CeO}_2$  nanocomposite were characterized by XRD, SEM and UV–vis DRS technique. For the photocatalytic redox reaction of CR in aqueous medium, the composite photocatalyst exhibits enhanced photocatalytic activity under UVA

light irradiation. The highest efficiency was observed at 30 wt %  $\text{p-CuBi}_2\text{O}_4$  content as a result of 83.05 % of photoactivity for 100 min under UVA light at pH 7 and 25 °C. The effective electron-hole separation at the bonded interfaces and in the two semiconductors was believed to be mainly responsible for the remarkably enhanced photocatalytic activity of 30 wt %  $\text{CuBi}_2\text{O}_4/\text{CeO}_2$  in the course of the photocatalytic redox conversion of CR. The mechanism of the increased photocatalytic activity of (30 wt %)  $\text{CuBi}_2\text{O}_4/\text{CeO}_2$  photocatalyst has been discussed by calculated energy band positions. The efficient electron-hole separation process in the p-n heterojunction semiconductors under UV light irradiation was considered to be mainly responsible for the obviously improved photocatalytic activity of (30 wt %)  $\text{CuBi}_2\text{O}_4/\text{CeO}_2$  catalyst in the course of the photocatalytic redox conversion of Congo red. These findings should be valuable for designing effectively photocatalyst and can be an alternative compound in a variety of areas, such as sensor technology, optical coatings, electrochromic materials and environment.

## REFERENCES

- [1] M. Mogensen, N. M. Sammes, G. A. Tompsett, Physical, « chemical and electrochemical properties of pure and doped ceria », *Solid State Ionic*, 129, 2000, pp. 63-64.
- [2] M. Yashima, S. Sasaki, Y. Yamaguchi, M. Kakihana, M. Yoshimura, T. Mori, « Internal distortion in  $ZrO_2$ - $CeO_2$  solid solutions: Neutron and high-resolution synchrotron x-ray diffraction study », *Applied Physics. Letter*, 72, 1998, pp.182.
- [3] K. Nikolaou, «Emissions reduction of high and low polluting new technology vehicles equipped with a  $CeO_2$  catalytic system » ,*Science and Total Environment*, 235, 1999, pp.71.
- [4] M. Ozawa, « Role of cerium-zirconium mixed oxides for car pollution » , *Journal of Alloy and Compounds* , 275/277, 1998, pp.886-890.
- [5] X. Feng, D. C. Sayle, Z.L.Wang, M. S. Paras, B. Santora, A. C. Sutorik, T. X. T. Sayle, Y. Yang, Y. Ding, X. Wang, Y. Her, « Converting Ceria Polyhedral Nanoparticles into Single-Crystal Nanospheres », *Science* 312, 2006, pp. 1504-1508.
- [6] N. Imanaka, T. Masui, H. Hirai, G. Adachi, «Amorphous cerium-titanium solid solution phosphate as a novel family of band gap tunable sunscreen materials » , *Chemical Materials*, 15 , 2003, pp.2289-2291
- [7] J. Zhou, D. R. Mullins, « Adsorption and reaction of formaldehyde on thin-film cerium oxide », *Surface Science*, 600, 2006, pp.1540-1546.
- [8] N. Kakuta,, N. Morishima, M. Kotobuki,T. Iwase, T. Mizushima, Y. Sato, S. Matsuura, « Oxygen Storage Capacity (OSC) of Aged Pt/ $CeO_2$ / $Al_2O_3$  Catalysts, Roles of Pt and  $CeO_2$  supported on  $Al_2O_3$  », *Applied Surface science*, 121/122 , 1997, pp.408-412.
- [9] M. Lira-Cantu, F. C. Krebs, « Hybrid solar cells based on MEH-PPV and thin film semiconductor oxides ( $TiO_2$ ,  $Nb_2O_5$ ,  $ZnO$ ,  $CeO_2$  and  $CeO_2$ - $TiO_2$ ): Performance improvement during long-time irradiation» *Solar Energy Material Solar Cells*, 90, 2006, pp. 2076-2086.
- [10] M. Flytzani-Stephanopoulos, M. Sakbodin, Z . Wang, « Regenerative Adsorption and Removal of  $H_2S$  from Hot Fuel Gas Streams by Rare Earth Oxides», *Science* 312, 2006, pp. 1508-1510.
- [11] A. H. Morshed, M. E. Moussa, S. M. Bedair, R. Leonard, S. X. Liu, N. El-Masry, «Violet/blue emission from epitaxial cerium oxide films on silicon substrates», *Applied Physical Letter*, 70, 1997, pp. 1647.
- [12]. N. Ozer, « Optical properties and electrochromic characterization of sol-gel deposited ceria films», *Solar Energy Material Solar Cells*, 68, 2001, pp. 391-400.
- [13] J.Q. Geng, Z.Y. Jiang, Y.B. Wang, D. Yang, «Carbon- modified  $TiO_2$  nanotubes with enhanced photocatalytic activity synthesized by a facile wet chemistry method», *Scripta Materialia*, 59, 2008, pp. 352-355.
- [14] I. Mora-Sero, J. Bisquert, T. Dittrich, A. Belaidi, A.S. Susha, A.L. Rogach, «Photosensitization of  $TiO_2$  layers with CdSe quantum dots: correlation between light absorption and photoinjection», *Journal Physical Chemistry C*, 111, 2007, pp. 14889-14892.
- [15] Z. Bian, J. Zhu, S. Wang, Y. Cao, X.Qian, H. Li, «Self assembly of active  $Bi_2O_3$ / $TiO_2$  visible photocatalyst with ordered mesoporous structure and highly crystallized anatase», *Journal Physical Chemistry C*, 112, 2008, pp.6258-6262.
- [16] C. Hu, Z. Zhang, H. Liu, P. Gao, Z.LinWang, «Direct synthesis and structure characterization of ultrafine  $CeO_2$  nanoparticles. *Nanotechnology*, 17, 2006, pp.5983-5987
- [17] G.K. Pradhan, K.M. Parida, « Fabrication of iron-cerium mixed oxide: an efficient photocatalyst for dye degradation» , *Internatinal Journal Engineering science Technology*, 2, 2010, pp.53-65.
- [18] W. Wu, S. Li, S. Liao, F. Xiang, X. Wu, « Preparation of new sunscreen materials  $Ce_{1-x}Zn_xO_{2-x}$  via solid-state reaction at room temperature and study on their properties. *Rares Metals*, 29, 2010, pp.149.
- [19] Małecka, M.A., Ke pin'ski, L., Mis'ta, W., « Structure evolution of nanocrystalline  $CeO_2$  and  $CeLnO_x$  mixed oxides ( $Ln = Pr, Tb, Lu$ ) in  $O_2$  and  $H_2$  atmosphere and their catalytic activity in soot combustion», *Applied Catalysis B*,74, 2007, pp. 290-298.
- [20] T. Cai, Y. Liao, Z. Peng, Y. Long, Z. Wei, Q. Deng, « Photocatalytic performance of  $TiO_2$  catalysts modified by  $H_3PW_{12}O_{40}$ ,  $ZrO_2$  and  $CeO_2$  », *Journal Environmental Science*, 21, 2009, pp. 997-1004.
- [21] G. Ranga Rao,H. Ranjan Sahu, « XRD and UV-Vis diffuse reflectance analysis of  $CeO_2$ - $ZrO_2$  solid solutions synthesized by combustion method », *Proc. Indian Academic Science*, 113, 2001, pp. 651-658.
- [22] X. Wu, S. Liu, D. Weng, F. Lin, « Textural-structural properties and soot oxidation activity of  $MnO_x$ - $CeO_2$  mixed oxides», *Catalysis Communication*, 12, 2011, pp. 345-348.
- [23] L. Lingzhi, Y. Bing, « $CeO_2$ - $Bi_2O_3$  nanocomposite: Two step synthesis,

- microstructure and photocatalytic activity», *Journal of Non-Crystalline Solids*, 355, 2009, pp. 776–779
- [24] I. Bhati, P. B. Punjabi, S. C. Ameta, «Photocatalytic degradation of fast green using nanosized  $\text{CeCrO}_3$ », *Macedonian Journal Chemistry and Chemical Engineering*, 29, 2010, pp.195–202.
- [25] H. R. Pouretedal, S. Basati, « Synthesis , charactrization and photocatalytic activity of  $\text{CeO}_2/\text{SBA-15}$  », *Iranian Journal of Catalysis*, 2, 2012, pp. 50-54.
- [26] R. M. Mohamed, E. S. Aazam, «Synthesis and Characterization of  $\text{CeO}_2\text{-SiO}_2$  Nanoparticles by Microwave-Assisted Irradiation Method for Photocatalytic Oxidation of Methylene Blue Dye», *International Journal of Photoenergy*, 2012, pp. 1-9.
- [27] S. Song, L. Xu, Z. He, H. Ying, J. Chen, X. Xiao, B. Yan, « Photocatalytic degradation of C.I. Direct Red 23 in aqueous solutions under UV irradiation using  $\text{SrTiO}_3/\text{CeO}_2$  composite as the catalyst », *Journal of Hazardous Materials*, 152, 2008, pp.1301–1308.
- [28] H. Wang, L. Yang, H. Yu, F. Peng, « A Highly Efficient and Stable Visible-Light Plasmonic Photocatalyst  $\text{Ag-AgCl/CeO}_2$ », *World Journal Nano Science Engineering*, 1, 2011, pp. 129-136.
- [29] N. Wetchakun, S. Chaiwichain, B. Inceesungvorn, K. Pingmuang, S. Phanichphant, A.I. Minett, J. Chen, «  $\text{BiVO}_4/\text{CeO}_2$  Nanocomposites with High Visible-Light-Induced Photocatalytic Activity», *Applied Material Interfaces*, 4, 2012, pp. 3718–3723.
- [30] R. Rangel, G.J. López Mercado, P. Bartolo-Pérez, R. García, « Nanostructured- $[\text{CeO}_2, \text{La}_2\text{O}_3, \text{C}]/\text{TiO}_2$  Catalysts for Lignin Photodegradation », *Science of Advance Materials*, 4, 2012, pp. 573–578.
- [31] N. Sabari Arul, D. Mangalaraj, P. C. Chen, N. Ponpandian, P. Meena, Y. Masuda, «Enhanced photocatalytic activity of cobalt-doped  $\text{CeO}_2$  nanorods », *Journal Sol-Gel Science Technology*, 64,2012, pp. 515–523.
- [32] A. Zhang, « Hydrothermal processing for obtaining of  $\text{BiVO}_4$  nanoparticles », *Journal of Material Letter*, 63, 2009, pp.1939–1942.
- [33] J. S. Valente, F. Tzomoantzi, J. Prince, « Highly efficient photocatalytic elimination of phenol and chlorinated phenols by  $\text{CeO}_2/\text{MgAl}$  layered double hydroxides », *Journal of Applied Catalysis B*, 102, 2011, pp. 276–285.
- [34] L. Li, B. J. Yan, «  $\text{CeO}_2\text{-Bi}_2\text{O}_3$  nanocomposite: Two step synthesis, microstructure and photocatalytic activity», *Journal Non-Crystalline Solids*, 355, 2009, pp 776–779.
- [35] N. Couselo, F.S.Garcia Einschlag, R.J. Candal, M. Jobbagy, «Tungsten-doped  $\text{TiO}_2$  vs pure  $\text{TiO}_2$  photocatalysts: effects on photobleaching kinetics and mechanism», *Journal Physical Chemistry C*, 112, 2008, pp.1094–1100.
- [36] A. Sasahara, C.L. Pang, H. Onishi, « Local work function of Pt clusters vacuum-deposited on a  $\text{TiO}_2$  surface », *Journal Physical Chemistry B*, 110, 2006, pp. 17584–17588.
- [37] A.Takeo, Y. Konishi, Y. Iwasaki, H. Sugihara, K. Sayama, « High-throughput screening using porous photoelectrode for the development of visible-lightresponsive semiconductors », *Journal Comb. Chemistry*, 9, 2007, pp. 574–581.
- [38] R. C. Pullar, M.D.Taylor, A.K. Bhattacharya, *Journal of the European Ceramic Society*, 18, 1988, pp.1759-1764.
- [39] K. Vasanth Kumar, K. Porkodi, F. Rocha, « Langmuir–Hinshelwood kinetics – a theoretical study, *Catal. Commun.* 9, 2008, pp. 82–84.
- [40] J. Keren, « Fabrication and Catalytic Property of Cerium Oxide Nanomaterials », *Thesis University of Nebraska – Lincoln*, 2011.
- [41] C. Hu, Z. Zhang, H. Liu, P. Gao, z. LinWang, Direct synthesis and structure characterization of ultrafine  $\text{CeO}_2$  nanoparticles», *Nanotechnology*, 17, 2006, pp. 5983–5987
- [42] K.S. Lin S. «Chowdhury, « Synthesis, Characterization, and Application of 1-D Cerium Oxide Nanomaterials: A Review», *International Journal of Molecular Science*, 11,2010, 3226-3251.
- [43] N. T. Hahn, V.C. Holmberg, B.A. Korgel,, C. B. Mullins, « Electrochemical Synthesis and Characterization of p- $\text{CuBi}_2\text{O}_4$  Thin Film Photocathodes», *Journal Physcal Chemistry C*, 116, 2012, pp. 6459–6466.
- [44] X. Lu, X. Li, F. Chen, C. Ni, Z. Chen «, Hydrothermal synthesis of prism-like mesocrystal  $\text{CeO}_2$ », *Journal Alloys Compound*, 476, 2012, pp. 958–962.
- [45] Y. Xu, M.A.A. Schoonen, «The absolute energy positions of conduction and bands of selected semiconducting minerals», *American Mineralogist*, 85, 2000, pp. 543-556.
- [46] G. Magesh, b. Viswanathan, r. Viswanathan, P.,TVaradarajan, K., « Photocatalytic behavior of  $\text{CeO}_2\text{-TiO}_2$  system for degradation of methylene blue», *Indian Journal chemistry* 8A, 2009, pp.480-488
- [47] K. Marunsek, « Electrical conductivity of sintered LMS ceramics», *Material Technology*, 43,2009, pp. 79–84.

- [48] W. Liu, S. Chen, H. Zhang, X. Yu, « Preparation, characterisation of p-n heterojunction photocatalyst  $\text{CuBi}_2\text{O}_4/\text{Bi}_2\text{WO}_6$  and its photocatalytic activities», *Journal Experimental Nano Science*, 6, 2011, pp. 102–120
- [49] K. S. Lin, S. Chowdhury, « Synthesis, Characterization, and Application of 1-D Cerium Oxide Nanomaterials: A Review», *International Journal of Molecular Science*, 11, 2010, pp. 3226-3251.
- [50] Y. I. Kim, S.J. Atherton, E.S. Brigham, T.E. Mallouk, «Sensitized layered metal oxide semiconductor particles for photochemical composite powders by spray pyrolysis and their visible-light-driven photocatalysis in gas-phase acetaldehyde decomposition», *Catalysis Today*, 93/95, 2004, pp. 895-901
- [53] L. Mingce, C. Weimin, C. Jun, Z. Baoxue, C. Xinye, W. Yahui, « Efficient Photocatalytic Degradation of Phenol over  $\text{Co}_3\text{O}_4/\text{BiVO}_4$  Composite under Visible Light Irradiation», *Journal Physic Chemistry B*, 110, 2006, pp.20211-20216.
- hydrogen evolution from nonsacrificial electron donors», *Journal Physical Chemistry*, 97, 1993, pp. 11802-11810.
- [51] M.A. Butler, D. S. Ginley, « Prediction of Flatband Potentials at Semiconductor-Electrolyte Interfaces from Atomic Electronegativities», *Journal Electrochemical Society*, 125, 1998, pp. 228-232.
- [52] D. Li, H. Haneda, N. Ohashi, S. Hishita, Y. Yoshikawa, « Synthesis of nanosized nitrogen-containing  $\text{MO}_x\text{-ZnO}$  (M = W, V, Fe)